
Article:

Chen, L. and de Borst, R. (2019) Cohesive fracture analysis using Powell-Sabin B-splines. International Journal for Numerical and Analytical Methods in Geomechanics, 43 (2). pp. 625-640. ISSN: 0363-9061

https://doi.org/10.1002/nag.2882

Received: 25 April 2018 | Revised: 26 September 2018 | Accepted: 2 November 2018
DOI: 10.1002/nag.2882

RESEARCH ARTICLE

WILEY

Cohesive fracture analysis using Powell-Sabin B-splines

Lin Chen | René de Borst

Department of Civil and Structural Engineering, University of Sheffield, Sheffield, UK

Correspondence
René de Borst, University of Sheffield, Department of Civil and Structural Engineering, Sheffield S1 3JD, UK.
Email: r.deborst@sheffield.ac.uk

Funding information
H2020 European Research Council, Grant/Award Number: 664734

Summary

Powell-Sabin B-splines, which are based on triangles, are employed to model cohesive crack propagation without a predefined interface. The method removes limitations that adhere to isogeometric analysis regarding discrete crack analysis. Isogeometric analysis requires that the initial mesh be aligned a priori with the final crack path to a certain extent. These restrictions are partly related to the fact that in isogeometric analysis, the crack is introduced in the parameter domain by meshline insertions. Herein, the crack is introduced directly in the physical domain. Because of the use of triangles, remeshing and tracking the real crack path in the physical domain is relatively standard. The method can be implemented in existing finite element programmes in a straightforward manner through the use of Bézier extraction. The accuracy of the approach to model free crack propagation is demonstrated by several numerical examples, including discrete crack modelling in an L-shaped beam and the Nooru-Mohamed tension-shear test.

KEYWORDS
Bézier extraction, cohesive zone model, fracture, Powell-Sabin B-splines

1 | INTRODUCTION

Discrete crack models are important for understanding and predicting fracture in quasi-brittle materials such as concrete, rocks, and ceramics.[1-3] For this class of materials, the failure process takes place over a finite zone where normal and shear tractions are transferred across the crack surface due to interlocking and friction. The cohesive zone model, introduced by Dugdale[4] and Barenblatt,[5] is commonly employed to model the process zone. In this model, the traction in the fracture process zone is related to the crack opening by a traction-opening law.[6,7] The cohesive zone model can be incorporated in the finite element method, and different approaches have been proposed, for instance, using interface elements,[8-10] remeshing[11,12] or extended finite element methods.[13-15] More recently, isogeometric analysis has also been introduced in the context of crack propagation analysis.[16-23]

In isogeometric analysis, a crack segment is represented by Non-uniform rational basis spline (NURBS) or T-spline basis functions.[24] An advantage of the method is that the local stress field is smoother and more accurate than when using standard finite elements. However, NURBS and T-splines have some limitations when modelling (cohesive) fracture, and a proper discrete representation of a discontinuity may not be feasible in some situations. Experience shows that when using NURBS or T-splines the initial mesh must be sufficiently aligned with the final crack path a priori, see Section 8 in a previous study.[23] Furthermore, the higher-order continuity of the basis functions in isogeometric analysis, which is so appealing and leads to vastly improved stress predictions, fails near crack tips and only C^0-continuity remains. The former restriction is due to the insertion of the crack segment in the parameter domain and the reparameterisation in the physical domain, see Section 8 in a previous study.[23]

In this contribution, we employ Powell-Sabin B-splines[25] for cohesive crack modelling without a predefined interface. Powell-Sabin B-splines are based on triangles, which allows a straightforward introduction of the crack path in the physical domain. Also, remeshing is standard since established algorithms for remeshing of triangles in the physical domain can be exploited. Moreover, the C^1 continuity of Powell-Sabin B-splines[26,27] does not break down at a crack tip, leading to stresses, which are smooth around the crack tip. Consequently, the stress field can be employed directly in a criterion for crack nucleation. Powell-Sabin B-splines are not isogeometric in the strict sense that the geometry can always be captured exactly, but they share with NURBS and T-splines the property that they can exploit standard finite element data structures by using Bézier extraction.

We start with a brief introduction of the cohesive zone model and a review of basic properties of Powell-Sabin B-splines. Section 3 discusses some implementation aspects. Next, we discuss the algorithm to insert a new crack segment, including the algorithm for remeshing after insertion of a crack segment. In Section 4, numerical examples are given, which demonstrate the versatility and accuracy of the method.

2 | GALERKIN APPROXIMATION OF COHESIVE ZONE MODEL

In a cohesive-zone model, a crack is considered to be an interface Γ_c in the physical domain Ω, see Figure 1. The model relates tractions on Γ_c to the crack opening and sliding across it. Infinitesimal strains and linear elastic material behaviour are assumed. We use Powell-Sabin B-splines for the trial functions in the solution space, and they are also used for the geometry parametrisation.

2.1 | Cohesive zone formulation

The crack opening $[\![\mathbf{u}]\!]$ is given in the global coordinate system (x_1, x_2). The crack sliding and opening in the local coordinate system (s, n) (Figure 1) are derived as:

$$[\![\boldsymbol{v}]\!] = \left([\![v_s]\!],\ [\![v_n]\!]\right)^{\mathrm{T}} = \mathbf{R}[\![\mathbf{u}]\!] = \mathbf{R}\left([\![u_{x_1}]\!],\ [\![u_{x_2}]\!]\right)^{\mathrm{T}}, \tag{1}$$

with $\mathbf{R}$ as the rotation matrix, eg.[17] The traction crack-opening relation,

$$\mathbf{t}_d = \mathbf{t}_d\left([\![\boldsymbol{v}]\!]\right), \tag{2}$$

sets the relation between the traction acting at Γ_c and the displacement jump across it. In the global coordinate system (x_1, x_2), the traction $\mathbf{t}$ is obtained from $\mathbf{t}_d$ following a standard transformation as follows:

$$\mathbf{t} = \mathbf{R}^{\mathrm{T}}\mathbf{t}_d. \tag{3}$$

The strong form of the equilibrium equations and the boundary conditions read as follows:

$$\begin{cases} \nabla \cdot \boldsymbol{\sigma} = \mathbf{0} & \text{on} \quad \Omega \\ \mathbf{u} = \hat{\mathbf{u}} & \text{on} \quad \Gamma_u \\ \boldsymbol{\sigma} \cdot \mathbf{n} = \hat{\mathbf{t}} & \text{on} \quad \Gamma_t \\ \boldsymbol{\sigma} \cdot \mathbf{n} = \mathbf{t}\left([\![\mathbf{u}]\!]\right) & \text{on} \quad \Gamma_c \end{cases}, \tag{4}$$

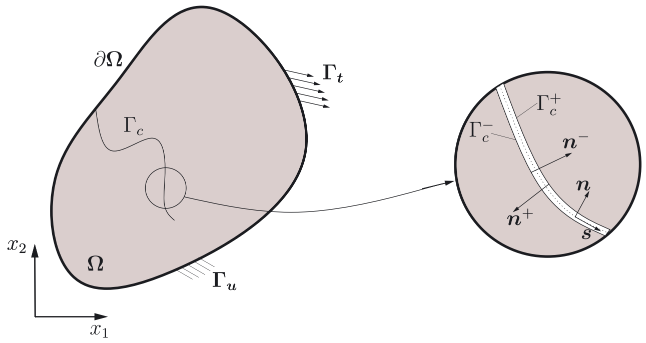

FIGURE 1 A solid body $\boldsymbol{\Omega}$ with an internal discontinuity Γ_c. Γ_c is an interface boundary with positive and negative sides, Γ_c^+, and Γ_c^-, respectively [Colour figure can be viewed at wileyonlinelibrary.com]

in which $\hat{\mathbf{u}}$ and $\hat{\mathbf{t}}$ represent prescribed displacements and tractions, respectively. $\mathbf{n}$ denotes the normal vector at the boundaries, and the Cauchy stress tensor $\boldsymbol{\sigma}$ relates to the infinitesimal strain $\boldsymbol{\varepsilon}$ as

$$\boldsymbol{\sigma} = \mathbf{D} : \boldsymbol{\varepsilon}, \tag{5}$$

with $\mathbf{D}$ the fourth-order elastic stiffness tensor.

2.2 | Powell-Sabin B-splines

We now give a concise description of Powell-Sabin B-splines. Reference is made to a previous study[28] for a more in-depth elaboration. We consider a triangulation $\mathcal{T}$ with $e = 1, 2, \cdots, E$ triangles and N_v vertices, which is denoted by thick black lines in Figure 2A. To construct Powell-Sabin B-splines, which are C^1-continuous, each triangle e is split into six $(n = 1, 2, \cdots, 6)$ mini-triangles, cf. Figure 2B. This leads to the Powell-Sabin refinement $\mathcal{T}^*$. For each vertex k of the triangulation $\mathcal{T}$, Powell-Sabin points are given in green as the vertex itself and points lying at the centre of the edges of $\mathcal{T}^*$. A Powell-Sabin triangle, drawn in red, is then defined for each vertex k. In order to obtain positive basis functions, the Powell-Sabin triangle is required to contain all the Powell-Sabin points. Herein, we employ the algorithm of a previous study[29] to find the minimum area triangle, which encloses the convex polygon defined by the Powell-Sabin points. For

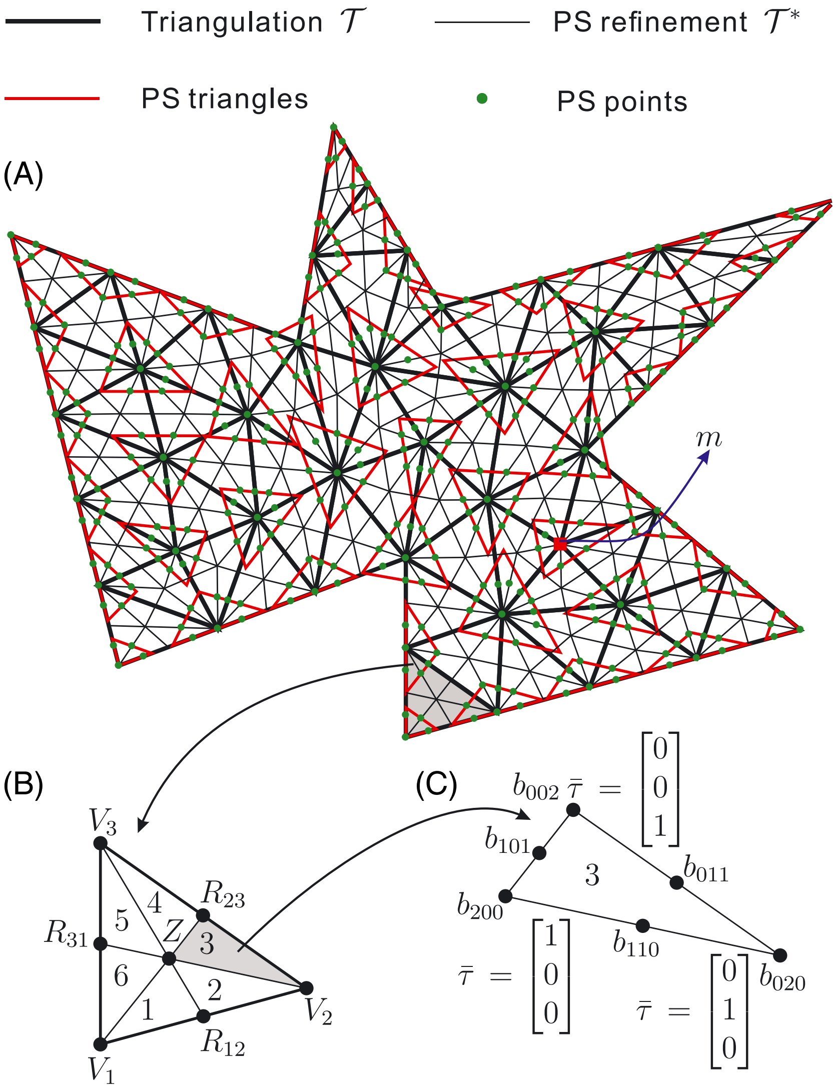

FIGURE 2 Example of a triangulation $\mathcal{T}$ (thick black lines), Powell-Sabin refinement $\mathcal{T}^*$ (thin black lines) of $\mathcal{T}$, Powell-Sabin triangles (red) and Powell-Sabin points (green). In B, each triangle e is subdivided into six mini-triangles. In C, each mini-triangle has a barycentric coordinate system $\bar{\tau}$ [Colour figure can be viewed at wileyonlinelibrary.com]

the Powell-Sabin triangles on the boundary, we will consider the following constraints: A, for an angle $\gamma < 180°$, two sides of the Powell-Sabin triangle must be aligned with the two boundary edges; B, for an angle $\gamma = 180°$, one side of the Powell-Sabin triangle must be aligned with the boundary edge, see Figure 2A.

Each triangle e of the triangulation $\mathcal{T}$ must be subdivided into six mini-triangles ($n = 1, 2, \cdots, 6$), Figure 2B. This yields the Powell-Sabin refinement $\mathcal{T}^*$. Each mini-triangle n has a barycentric coordinate system $\bar{\boldsymbol{\tau}} = \begin{bmatrix} \bar{\tau}_1 & \bar{\tau}_2 & \bar{\tau}_3 \end{bmatrix}^{\mathrm{T}}$ and Bézier ordinates $b_{r,s,t}$, cf. Figure 2C. Three Powell-Sabin B-splines $N_k^j, j = 1, 2, 3$, are defined on each vertex k with coordinate $\boldsymbol{V}_k = \left(x_1^k, x_2^k\right)$, ie, one for each corner of the Powell-Sabin triangle of vertex k. The Powell-Sabin B-splines N_k^j over each mini-triangle, Figure 2C, can then be expressed using the Bézier ordinates $b_{r,s,t}$ as

$$N_k^j\left(\bar{\boldsymbol{\tau}}\right) = \sum_{r+s+t=2} b_{r,s,t} B_{r,s,t}^2\left(\bar{\boldsymbol{\tau}}\right), \tag{6}$$

where $B_{r,s,t}^2\left(\bar{\boldsymbol{\tau}}\right)$ represent the Bernstein polynomials

$$B_{r,s,t}^2\left(\bar{\boldsymbol{\tau}}\right) = \frac{2!}{r!s!t!}\bar{\tau}_1^r\bar{\tau}_2^s\bar{\tau}_3^t. \tag{7}$$

The Bézier ordinates $b_{r,s,t}$ are obtained by first considering the following properties:

$$N_k^j\left(\boldsymbol{V}_l\right) = 0, \qquad \frac{\partial}{\partial x_1}N_k^j\left(\boldsymbol{V}_l\right) = 0, \qquad \frac{\partial}{\partial x_2}N_k^j\left(\boldsymbol{V}_l\right) = 0, \tag{8}$$

for any vertex $\boldsymbol{V}_k \neq \boldsymbol{V}_l$, and we denote

$$N_k^j\left(\boldsymbol{V}_k\right) = \alpha_k^j, \qquad \frac{\partial}{\partial x_1}N_k^j\left(\boldsymbol{V}_k\right) = \beta_k^j, \qquad \frac{\partial}{\partial x_2}N_k^j\left(\boldsymbol{V}_k\right) = \gamma_k^j. \tag{9}$$

To form a partition of unity on the domain, we must require

$$\sum_{j=1}^{3}\alpha_k^j = 1, \qquad \sum_{j=1}^{3}\beta_k^j = 0, \qquad \sum_{j=1}^{3}\gamma_k^j = 0, \tag{10}$$

and the coefficients α_k^j, β_k^j, and γ_k^j are subsequently obtained by solving the linear system

$$\begin{bmatrix} \alpha_k^1 & \alpha_k^2 & \alpha_k^3 \\ \beta_k^1 & \beta_k^2 & \beta_k^3 \\ \gamma_k^1 & \gamma_k^2 & \gamma_k^3 \end{bmatrix}\begin{bmatrix} x_1^{k,1} & x_2^{k,1} & 1 \\ x_1^{k,2} & x_2^{k,2} & 1 \\ x_1^{k,3} & x_2^{k,3} & 1 \end{bmatrix} = \begin{bmatrix} x_1^k & x_2^k & 1 \\ 1 & 0 & 0 \\ 0 & 1 & 0 \end{bmatrix} \tag{11}$$

in which, $\boldsymbol{Q}_k^j = \left(x_1^{k,j}, x_2^{k,j}\right)$ are coordinates of the Powell-Sabin triangle corners associated with each vertex k. Having obtained the coefficients α_k^j, β_k^j, and γ_k^j we can compute the Bézier ordinates of each mini-triangle n in element e.

We next arrange the Bézier ordinates in a matrix form $\boldsymbol{C}_n^e$ and denote the Powell-Sabin B-splines associated with each mini-triangle n in element e by $\boldsymbol{N}_n^e$. To implement the method in existing finite element codes, Bézier extraction is used as follows:

$$\boldsymbol{N}_n^e = \boldsymbol{C}_n^e\boldsymbol{B}, \tag{12}$$

over each mini-triangle n in element e with six Bernstein polynomials, contained in the vector $\boldsymbol{B}$.[28] Figure 3 gives an example of three Powell Sabin B-splines associated with vertex m in Figure 2A.

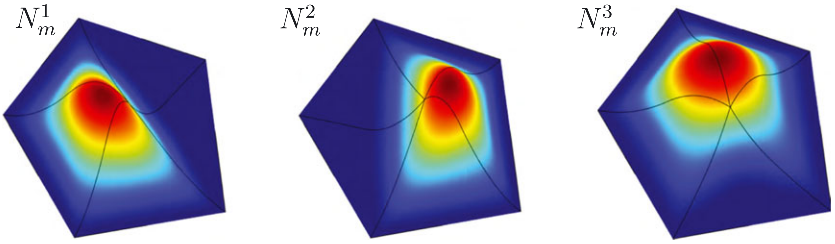

FIGURE 3 Example of three Powell-Sabin B-splines associated with vertex m in Figure 2A [Colour figure can be viewed at wileyonlinelibrary.com]

2.3 | Finite element discretisation

We employ Powell-Sabin B-splines for the description of the geometry as well as for the interpolation of the displacement field as follows:

$$\mathbf{x} = \sum_{k=1}^{N_v}\sum_{j=1}^{3} N_k^j \boldsymbol{X}_k^j, \qquad \mathbf{u} = \sum_{k=1}^{N_v}\sum_{j=1}^{3} N_k^j \boldsymbol{U}_k^j, \tag{13}$$

where $\boldsymbol{X}_k^j$ represents the coordinates of the Powell-Sabin triangle corners, $\boldsymbol{Q}_k^j$; $\boldsymbol{U}_k^j$ denotes the degrees of freedom at $\boldsymbol{Q}_k^j$, and N_v is the total number of vertices.

To solve the equilibrium equation, Equation 4, it is cast in a weak form as follows:

$$\int_{\Omega} \delta\boldsymbol{\varepsilon} : \boldsymbol{\sigma}\mathrm{d}\Omega + \int_{\Gamma_c} \delta[\![\mathbf{u}]\!] \cdot \mathbf{t}([\![\mathbf{u}]\!])\,\mathrm{d}\Gamma = \int_{\Gamma_t} \delta\mathbf{u}\cdot\hat{\mathbf{t}}\mathrm{d}\Gamma \qquad \forall\delta\mathbf{u} \in \nu_0, \tag{14}$$

where $\delta\boldsymbol{\varepsilon}$, $\delta\mathbf{u}$, and $\delta[\![\mathbf{u}]\!]$ are the virtual strain, the virtual displacement, and the virtual relative displacement fields, respectively, and $\nu_0 = \left\{\boldsymbol{\nu} : \nu_i \in H^1(\Omega), \nu_i | \Gamma_D = 0\right\}$; H^1 is denoting the first-order Sobolev space.

Using small-strain kinematics and considering the Powell-Sabin approximation Equation 13, the weak form Equation 14 yields:

$$\mathbf{f}_{\mathrm{int}}(\mathbf{u}) = \mathbf{f}_{\mathrm{ext}}, \tag{15}$$

with

$$\mathbf{f}_{\mathrm{int}}(\mathbf{u}) = \int_{\Omega} \mathbf{B}^{\mathrm{T}}\boldsymbol{\sigma}\mathrm{d}\Omega + \int_{\Gamma_c} \mathbf{H}^{\mathrm{T}}\mathbf{t}([\![\mathbf{u}]\!])\,\mathrm{d}\Gamma \qquad \mathbf{f}_{\mathrm{ext}} = \int_{\Gamma_t} \mathbf{N}^{\mathrm{T}}\hat{\mathbf{t}}\mathrm{d}\Gamma. \tag{16}$$

The matrices $\mathbf{N}$, $\mathbf{B}$, and $\mathbf{H}$ contain shape functions, their derivatives, and relative displacements, respectively.[21]

Linearisation gives the tangential stiffness matrix as follows:

$$\mathbf{K}_{\mathrm{tan}} = \int_{\Omega} \mathbf{B}^{\mathrm{T}}\mathbf{D}\mathbf{B}\mathrm{d}\Omega + \int_{\Gamma_c} \mathbf{H}^{\mathrm{T}}\mathbf{R}^{\mathrm{T}}\mathbf{T}_d\mathbf{R}\mathbf{H}\mathrm{d}\Gamma, \tag{17}$$

where $\mathbf{T}_d$ is the tangent stiffness of traction-opening law at the interface[17]

$$\mathbf{T}_d = \frac{\partial\mathbf{t}_d}{\partial[\![\boldsymbol{\nu}]\!]}. \tag{18}$$

3 | NUMERICAL IMPLEMENTATION

We now outline some relevant implementation aspects. First, we introduce the refinement procedure for cohesive crack growth. After the insertion of a crack segment, elements with bad aspect ratios may be generated in the vicinity of the new crack tip. Below, we propose a remeshing algorithm for a domain, which contains such elements. This is followed by a discussion on how to map the displacement vector and the history variables onto the new mesh.

3.1 | Adaptive analysis for cohesive crack growth

By virtue of the C^1-continuity of Powell-Sabin B-splines at the crack tip, one can check the crack initiation criterion at this point (A in Figure 4A), which in this case means directly compare the major principal stress σ_1 with the tensile strength t_u. When the initiation criterion is violated, a crack is inserted through the entire element e_0, see Figure 4B. The new crack tip is now at C. Due to lack of information about the possible curvature of the crack, it is introduced as a straight line within the element.

While the stress computation is more accurate when using Powell-Sabin B-splines, the direction of crack propagation is very sensitive, and the quality of the prediction of the direction of crack propagation can be improved further by an averaging procedure.[23] An averaged stress tensor is computed using a Gaussian weight function[13]

$$w = \frac{1}{(2\pi)^{\frac{3}{2}}l^3}\exp\left(-\frac{r^2}{2l^2}\right), \tag{19}$$

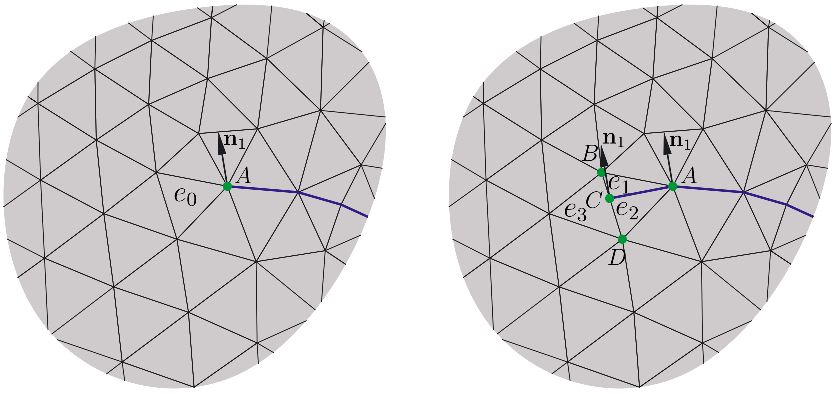

(A) intial crack (B) crack propagation

FIGURE 4 Crack path after crack propagation. The mesh is shown before remeshing in the deformed configuration. The blue curve denotes the crack interface Γ_c. Point A denotes the old crack tip, while point C is the new crack tip [Colour figure can be viewed at wileyonlinelibrary.com]

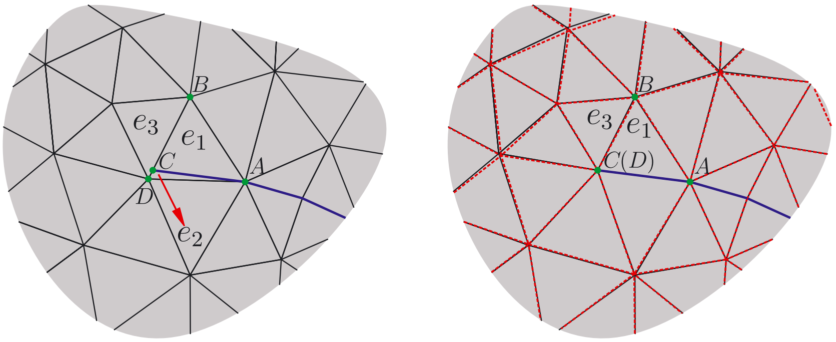

(A) crack propagation (B) element adjustment

FIGURE 5 Element adjustment after crack propagation for the case of either a small or a large line ratio ζ. The mesh is shown before (black solid lines) and after (red dotted lines) remeshing. The blue curve denotes the crack Γ_c. Point A locates the old crack tip, while point C is the new crack tip [Colour figure can be viewed at wileyonlinelibrary.com]

with l is a smoothing length, typically taken around three times a representative element size, and r is the distance to the crack tip. The normal vector to the crack $\mathbf{n}_1$ is subsequently computed on the basis of this averaged stress tensor, see Figure 4B.

Upon insertion of a new crack segment, element e_0 is divided into two triangles e_1 and e_2, see Figure 4B. Because of the insertion of a new crack tip, C, the triangular element e_3 has four vertices. This is not allowed for Powell-Sabin B-splines[25] and we need to remesh, see Figures 5B and 6B. Herein, we consider two cases of element reconstruction, depending on the ratio $\zeta = |BC| / |CD|$, see Figures 5 and 6. $|BC|$ and $|CD|$ are the lengths of the line segments BC and CD, respectively.

Case 1: If ζ is too small or large, $\zeta < 0.5$ or $\zeta > 2$, point C will be close to either point B or point D. This renders either element $e1$ or $e2$ with a bad aspect ratio. To remedy this, we merge point C with the closest point between points B and D. In Figure 5B, we attach point D to point C to match the crack path. Elements $e1$ and $e3$ are then unchanged. Because of the movement of point D, we must remesh $\mathbf{\Omega}$ in order to avoid elements with bad aspect ratios, which will be treated next, Section 3.2. The meshes in the deformed configuration are denoted by solid and dotted lines, respectively, in Figure 5B before and after remeshing.

Case 2: If the ratio ζ is moderate, $0.5 \leq \zeta \leq 2$, point C will be in the central part between points B and D. Elements $e1$ and $e2$ will then have similar aspect ratios. Consequently, the elements $e1$ and $e2$ should be kept, Figure 6B. To eliminate the element with four vertices, ie, element $e3$ in Figure 6A, we subdivide it into two subelements: elements $e4$ and $e5$ in Figure 6B. After crack insertion, newly generated elements, such as $e1$, $e2$, $e4$, and $e5$, usually do not have a good aspect ratio, eg, Figure 6B. To make them suitable for analysis, $\mathbf{\Omega}$ must be remeshed, as will be discussed next. The dotted lines in Figure 6B show the mesh after remeshing.

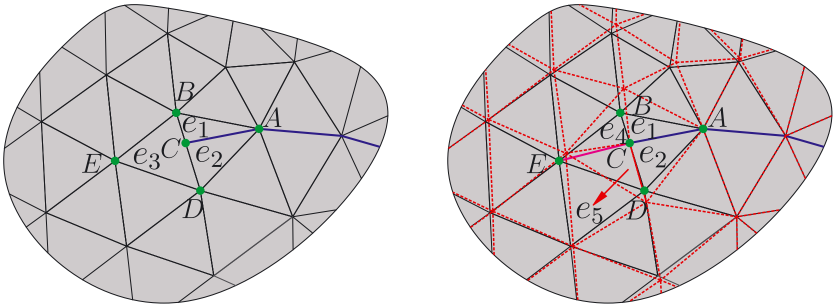

(A) crack propagation (B) element adjustment

FIGURE 6 Element adjustment after crack propagation for the case of moderate line ratio ζ. Here, the meshes in the deformed configuration before (black solid lines) and after (red dotted lines) remeshing are shown. The blue solid curve denotes the crack interface Γ_c. Point A denotes the old crack tip, while point C is the new crack tip location [Colour figure can be viewed at wileyonlinelibrary.com]

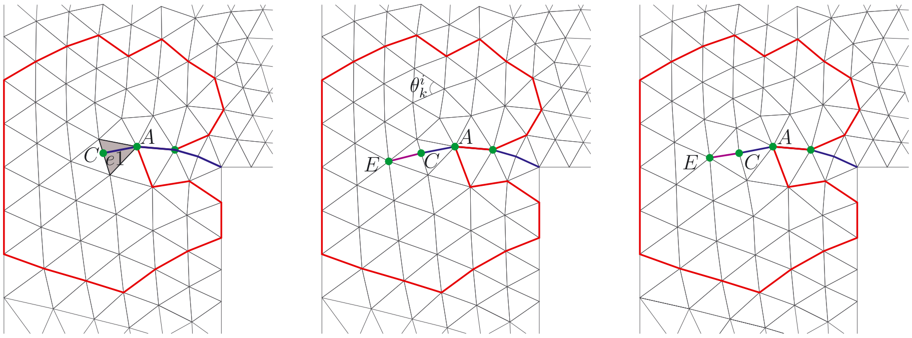

(A) crack propagation (B) element adjustment (C) domain remesh

FIGURE 7 Mesh in the deformed configuration before and after remeshing. The blue solid curve denotes the crack interface Γ_c. Point A gives the old crack tip, while point C denotes the new crack tip. Segment AC represents the new crack interface [Colour figure can be viewed at wileyonlinelibrary.com]

3.2 | Remeshing of a body after crack insertion

After the insertion of a crack segment, the aspect ratio of triangular elements near the new crack tip has generally changed, Figures 5 and 6. This requires remeshing to arrive at all elements having an analysis-suitable aspect ratio, while not changing the vertices along the crack path. There are mainly two approaches for remeshing: mesh adaptation strategies[30,31] and parametrisation techniques.[23,32-34] Mesh adaptation strategies employ local mesh modifications to adapt the mesh to a given mesh size criterion and to improve the input mesh quality. In parametrisation techniques, the input mesh serves as a support for building a continuous parametrisation of the surface. The initial surface is parametrised onto a surface, which is meshed using any standard planar mesh generation procedure. Then, the new triangulation is mapped back to the original surface.[35] In this study, the mesh adaptation strategy will be followed.

Inserting a new crack segment affects only elements around the crack tip, but will not influence the domain away from the crack tip. As an example, only the area Ω_R inside the red polygon of Figure 7 needs to be remeshed. Vertices on and outside the red polygon and the crack tips will not move. Herein, the area Ω_R to be remeshed is determined as follows: It starts at the element with the newly inserted crack segment (the grey element $e1$ in Figure 7), and then a radial marching is done until three elements have been crossed in all directions, see Figure 7. Next, we exclude the elements along one side of the crack interface. In Figure 7, this applies to the elements along the lower side of the crack interface.

To remesh Ω_R, in the example of Figure 7, the area inside the red polygon, we must fix the vertices on the polygon and along the crack path. Herein, the vertices are set by requiring that the minimum interior angle $\theta^1_{\min}$ be maximised of all triangles inside Ω_R as follows:

$$\begin{aligned} &\max && \theta^1_{\min} \\ &\text{subject to:} && \theta^i_k \geq \theta^1_{\min} \quad \text{and} \quad \theta^1_{\min} \geq \pi/6, \end{aligned} \tag{20}$$

where θ^i_k is the ith interior angle ($i = 1, 2, 3$) of triangle k, see Figure 7B. In this study, the MATLAB function *fmincon* is used to find the optimum in Equation 20.[36] Alternatively, one can use optimisation packages like MOSEK[37] or ALGLIB,[38] which may provide a better efficiency for large-scale problems. After obtaining the minimum interior angle $\theta^1_{\min}$, we can further remesh by using Equation 20 to maximise the second minimum interior angle $\theta^2_{\min}$ of all triangles inside Ω_R. This procedure can be repeated until all interior angles have attained a maximum value.

3.3 | Update of the displacement vector and the history variables

During crack propagation, new elements and vertices are introduced, and after the insertion of a new crack segment, remeshing of Ω_R is necessary to ensure that elements have a suitable aspect ratio. This evidently results in modifying the mesh in Ω_R. As a consequence, Powell-Sabin B-spline functions must be computed on the new triangles and the displacements ${}^t\mathbf{U}$ from previous time step t have to be transferred to provide the initial values ${}^{t+\Delta t}_{0}\mathbf{U}_r$ at time step $t+\Delta t$. $\mathbf{U}$ and $\mathbf{U}_r$ are displacements associated with the mesh before and after remeshing Ω_R, respectively. Herein, a least-squares fit is employed to carry out the mapping of ${}^t\mathbf{U}$ to ${}^{t+\Delta t}_{0}\mathbf{U}_r$. This is achieved by minimising

$$\psi = \int_{\Omega_R} \left\| {}^{t+\Delta t}_{0}\mathbf{u}_r - {}^t\mathbf{u} \right\| \mathrm{d}\Omega = \int_{\Omega_R} \left\| {}^{t+\Delta t}\mathbf{N}_r \, {}^{t+\Delta t}_{0}\mathbf{U}_r - {}^t\mathbf{u} \right\| \mathrm{d}\Omega, \tag{21}$$

in which $\mathbf{u}$ and $\mathbf{u}_r$ are displacements, and ${}^{t+\Delta t}\mathbf{N}_r$ denotes the basis functions associated with the domain after remeshing Ω_R at time step $t+\Delta t$. Minimising Equation 21 with respect to ${}^{t+\Delta t}_{0}\mathbf{U}_r$ yields

$$\mathbf{M} \, {}^{t+\Delta t}_{0}\mathbf{U}_r = \mathbf{p}, \tag{22}$$

with

$$\mathbf{M} = \int_{\Omega_R} \left({}^{t+\Delta t}\mathbf{N}_r\right)^{\mathrm{T}} {}^{t+\Delta t}\mathbf{N}_r \mathrm{d}\Omega, \tag{23}$$

which is obtained directly by Gaussian quadrature at each element on the domain after remeshing Ω_R at time step $t+\Delta t$, and

$$\mathbf{p} = \int_{\Omega_R} \left({}^{t+\Delta t}\mathbf{N}_r\right)^{\mathrm{T}} {}^t\mathbf{u} \mathrm{d}\Omega = \int_{\Omega_R} \left({}^{t+\Delta t}\mathbf{N}_r\right)^{\mathrm{T}} \left({}^t\mathbf{N}\right) {}^t\mathbf{U} \mathrm{d}\Omega, \tag{24}$$

where the integration is carried out at each element on the domain before remeshing Ω_R at time step t. ${}^t\mathbf{N}$ represents basis functions associated with the domain before remeshing Ω_R.

4 | NUMERICAL EXAMPLES

Below, we will consider three examples. While the last two examples demonstrate the ability of the method to analyse the propagation of curved cracks, the first example is used to assess the accuracy and convergence of the adaptive remeshing needed for the crack propagation. To this end, a Poisson problem is considered for which an analytical solution exists.[39]

4.1 | Poisson problem on an L-shaped domain

The Poisson problem is solved on an L-shaped domain, Figure 8A. The L-shaped domain is defined as $\Omega_L = \{(-1,1)\times(-1,1)\} \setminus \{(0,1)\times(0,1)\}$. The problem is defined by the following governing equation and boundary conditions:

$$\triangle u = 0, \qquad \frac{\partial \bar{u}}{\partial n} = g \quad \text{on} \quad \Gamma_N, \qquad \bar{u} = 0 \quad \text{on} \quad \Gamma_D, \tag{25}$$

with u as a scalar variable, eg, the temperature. The exact solution is given by

$$u = r^{\frac{2}{3}} \sin \frac{2\phi - \pi}{3}, \qquad \phi = (0, 2\pi], \tag{26}$$

The domain is modelled by a single C^1 continuous Powell-Sabin B-spline patch, Figure 8B. To impose the Dirichlet boundary condition for the Powell-Sabin triangles, the algorithm proposed in a previous study[40] is employed. The Neumann condition is imposed implicitly. To locally refine the triangulation we use the method of another study,[41] see

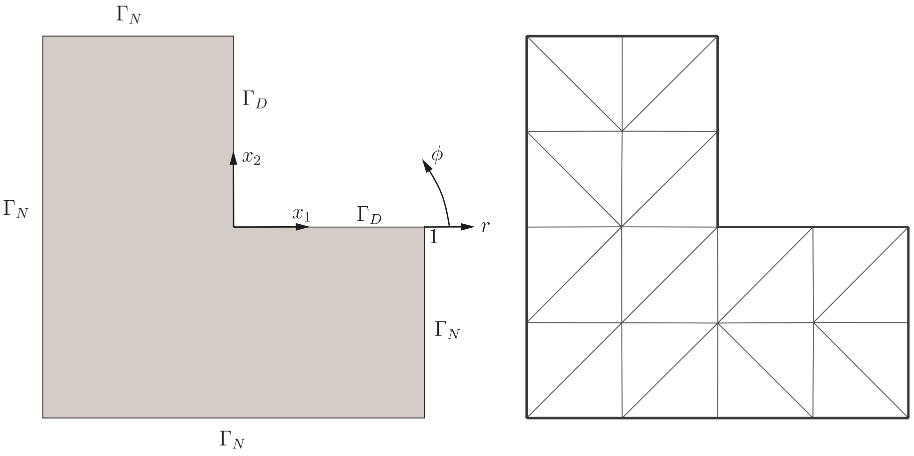

(A) problem definition of the plate (B) Initial triangulation

FIGURE 8 Poisson problem on an L-shaped domain: problem definition and initial triangulation [Colour figure can be viewed at wileyonlinelibrary.com]

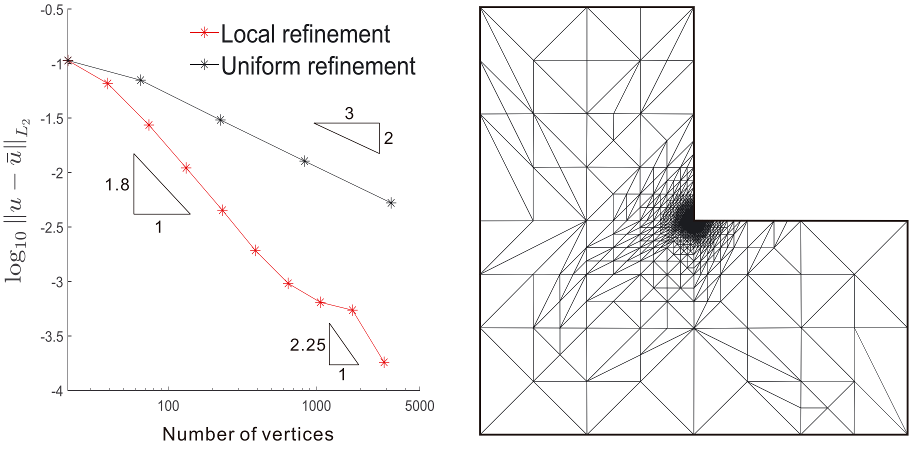

(A) L_2 error norm (B) mesh after adaptive refinement

FIGURE 9 Poisson problem on an L-shaped domain: L_2 error norm and mesh after adaptive refinement [Colour figure can be viewed at wileyonlinelibrary.com]

Figure 9B. The error indicator of each element is computed using the L_2 error norm $\|u - \bar{u}\|_{L_2(\Omega_e)}$, where u stands for the exact solution and $\bar{u}$ denotes the approximate solution . The relative error ε_e of each element, needed for marking elements for refinement, is computed as[42-44]

$$\varepsilon_e = \frac{\|u - \bar{u}\|_{L_2(\Omega_e)}}{\sqrt{\left(\int_{\Omega_e} u^{\mathrm{T}} \cdot u \, d\Omega\right)}}. \tag{27}$$

Because of the singularity at the re-entrant corner $(x_1, x_2) = (0, 0)$, the rate of convergence k in the L_2 norm with respect to the total number of degrees of freedom is governed by the angle β ($\beta = \pi/2$) of the re-entrant corner[45]

$$k = -\min\left(p, \frac{\pi}{2\pi - \beta}\right) = -\min\left(p, \frac{2}{3}\right) = -\frac{2}{3} \tag{28}$$

Elements are marked for adaptive refinement through quantile marking ($\eta = 0.2$).[46] After adaptive refinement, we obtain the triangulation in Figure 9B. The error indicator has clearly identified the corner singularity.[46] In Figure 9A, we compare the error norm for uniform and adaptive refinement. For uniform refinement, the corresponding rate of convergence is $k = -2/3$. The optimal rate of convergence, $k = -2$, can be recovered by adaptive refinement. In the end of the convergence plot, the convergence rate is even higher than −2, see Figure 9A. It shows that the error level for adaptive refinement is smaller than that for uniform refinement. This is because adaptive refinement smoothens the gradient around the re-entrant corner, Figure 9B.

4.2 | L-shaped beam peeling test

In the next two examples, a linear isotropic material law is used for the bulk material. An exponential decohesion relation[13] is used for the constitutive behaviour in the crack

$$\begin{cases} t_n = t_u \exp\left(-\frac{t_u}{\mathcal{G}_c}\kappa\right) \\ t_s = d_{\text{int}} \exp\left(h_s \kappa\right) [\![v_s]\!] . \end{cases} \tag{29}$$

The history parameter κ is set through a loading function $f = f([\![v_n]\!], [\![v_s]\!], \kappa)$, which evolves according to Kuhn-Tucker conditions.[16]

$$f = [\![v_n]\!] \,\text{or}\, [\![v_s]\!] - \kappa \leqslant 0 \qquad \dot{\kappa} \geqslant 0 \qquad \dot{\kappa} f = 0. \tag{30}$$

In the case of unloading ($f < 0$), the tractions are obtained from a secant relation, as is customary in damage mechanics. To avoid interpenetration, a penalty stiffness $k_p = 10^5$MPa/mm is specified in the normal direction.

An L-shaped concrete panel is considered first. A vertical concentrated load is applied on the panel, see Figure 10A. The test has been reported in a previous study[47] and numerical simulations of crack propagation were presented in another study.[48] The following values for the material parameters were adopted: Young's modulus $E = 20$GPa, Poisson's ratio $\nu = 0.18$, tensile strength $t_u = 2.5$MPa, and fracture energy $\mathcal{G}_c = 0.13$ N/mm. Here, we only consider mode-I fracture, ie, $d_{\text{int}} = 0$ in Equation 29. Plane-stress conditions are assumed. Displacement control has been adopted to fully track the load-displacement path with steps of 0.01mm. Initially, the beam has been discretised by the triangulation presented in Figure 10B. The Powell-Sabin B-splines are employed to describe the geometry and to interpolate the displacements. The Dirichlet boundary condition is imposed using linear constraints, see Figure 11. Along the bottom edge, ed_1, (Figure 10A), the boundary condition is set as

$$\boldsymbol{U}_A = \mathbf{u}\left(\mathbf{x}_A\right), \qquad \boldsymbol{U}_B = \mathbf{u}\left(\mathbf{x}_B\right), \qquad \boldsymbol{U}_C = \mathbf{u}\left(\mathbf{x}_C\right), \qquad \text{etc.} \tag{31}$$

in which $\boldsymbol{U}$ is the degrees of freedom at Powell-Sabin triangle corner. $\mathbf{u}$ stands for the exact solution and $\mathbf{x}$ represents the coordinates of the Powell-Sabin triangle corner.

In the analysis displacement control is employed to apply the external load. The displacement boundary condition for the Powell-Sabin triangle t_1 associated with the load point E, Figure 11B, is approximated as

$$\boldsymbol{U}_D = \bar{\mathbf{u}}\left(\mathbf{x}_E\right), \qquad \boldsymbol{U}_F = \bar{\mathbf{u}}\left(\mathbf{x}_E\right), \tag{32}$$

where $\boldsymbol{U}$ denotes the degrees of freedom at the Powell-Sabin triangle corner. $\bar{\mathbf{u}}\left(\mathbf{x}_E\right)$ is the applied displacement at the loading point $\mathbf{x}_E$. This approximation may influence the stress and displacements near the loading point. However, according to Saint-Venant's principle, the influence on the far-field will be small.

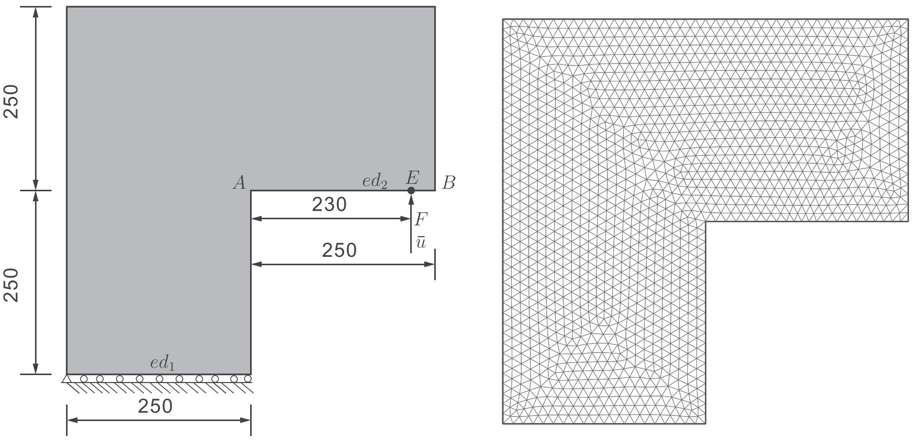

(A) geometry (in mm) and boundary conditions

(B) initial triangulation

FIGURE 10 L-shaped beam subject to a vertical load

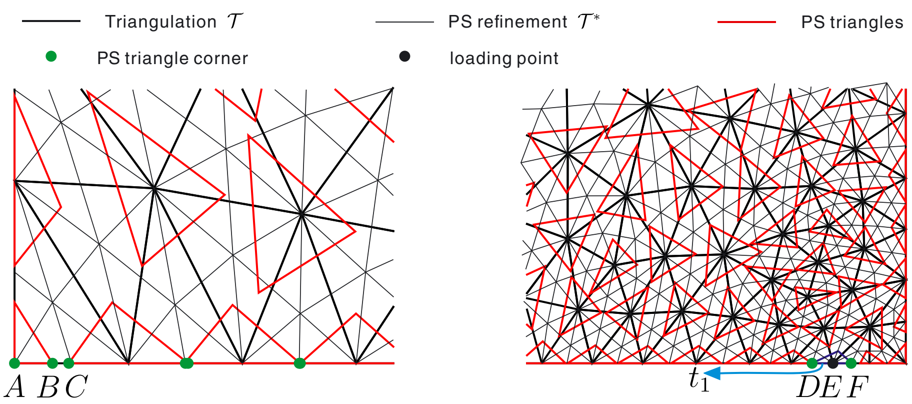

(A) along bottom edge ed_1 (B) along loading edge ed_2

FIGURE 11 Application of Dirichlet boundary conditions to the Powell-Sabin triangle corner along A, bottom edge ed_1 and B, loading edge ed_2 in Figure 10A [Colour figure can be viewed at wileyonlinelibrary.com]

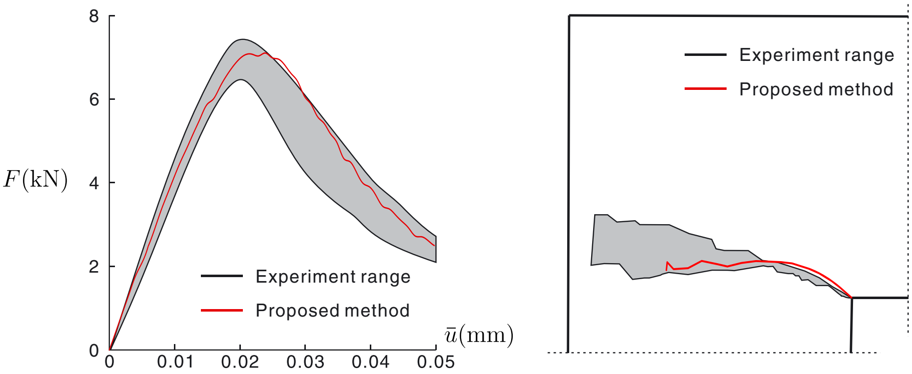

(A) load displacement curve (B) predicted crack path

FIGURE 12 Load-displacement response and predicted crack path [Colour figure can be viewed at wileyonlinelibrary.com]

The computed load-displacement curve is shown in Figure 12A. A good agreement is obtained with experimental data.[47] The curve exhibits some kinks due to a sudden release of the node at the crack tip when the fracture criterion is met. Upon mesh refinement, the kinks gradually disappear. Figure 12B shows that the computed crack path is well within the range recorded in the experiments.[47] In Figure 13, the meshes are given for different loading steps. The meshes are well defined with good aspect ratios, which demonstrates the soundness of the remeshing algorithm in Section 3.2. Figure 14 gives contour plots of the principal stress σ_1 for two different load levels. The stresses are smooth due to the C^1-continuity of the Powell-Sabin B-splines. The crack propagates smoothly through the interface Γ_c and no stress oscillations are observed. Figure 12B shows that there are also kinks in the crack path. Again, this is due to quadrature errors and the discretisation, and has also been observed in other higher continuity numerical approaches.[49] The kinks gradually disappear upon mesh refinement.

4.3 | Nooru-Mohamed tension shear test

This example serves to demonstrate the improvements for discrete crack propagation, which the use of Powell-Sabin B-splines offers over NURBS or T-splines.[16,23] The Nooru-Mohamed tension-shear test is considered. In a previous study,[23] this fracture test has been used to demonstrate limitations of the use of NURBS or T-splines for crack simulation. The Nooru-Mohamed tension-shear test has been carried out on a double-edge notched plane concrete specimen with a thickness of 50 mm.[50] Figure 15A shows the geometry and the boundary conditions. In the test, the specimen is first subjected to a prescribed horizontal displacement u_1 until a certain level of shear force F_1 is reached. Subsequently, a vertical load F_2 was applied on the top edge via displacement control while keeping F_1 constant. Three shear force values were tested: $F_1 = 5\mathrm{kN}$, $F_1 = 10\mathrm{kN}$, and $F_1 = 27.5\mathrm{kN}$. Here, we take the case $F_1 = 10\mathrm{kN}$, see Figure 15A. The elastic material parameters are: Young's modulus $E = 30\mathrm{GPa}$ and Poisson's ratio $\nu = 0.2$. To describe the fracture process, we employ

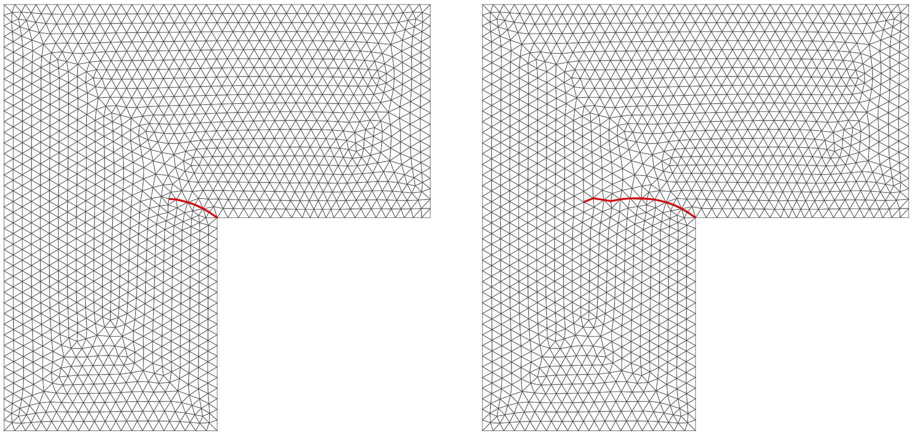

(A) mesh at load step $\bar{u} = 0.23\text{mm}$ (B) mesh at load step $\bar{u} = 0.31\text{mm}$

FIGURE 13 Mesh in the deformed configuration. The red lines indicate the crack path, which is aligned with the triangle element boundaries [Colour figure can be viewed at wileyonlinelibrary.com]

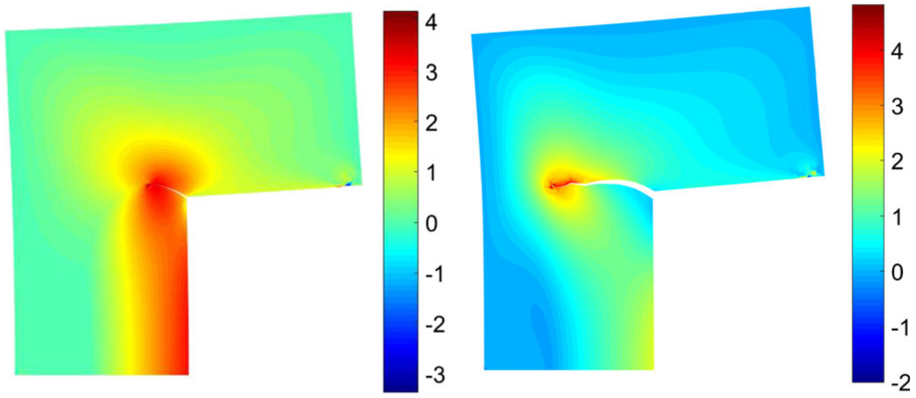

(A) σ_1 contour plot for $\bar{u} = 0.23\text{mm}$ (B) σ_1 contour plot for $\bar{u} = 0.34\text{mm}$

FIGURE 14 Stress distribution σ_1(MPa) for different load steps. The displacements have been amplified by a factor 100 [Colour figure can be viewed at wileyonlinelibrary.com]

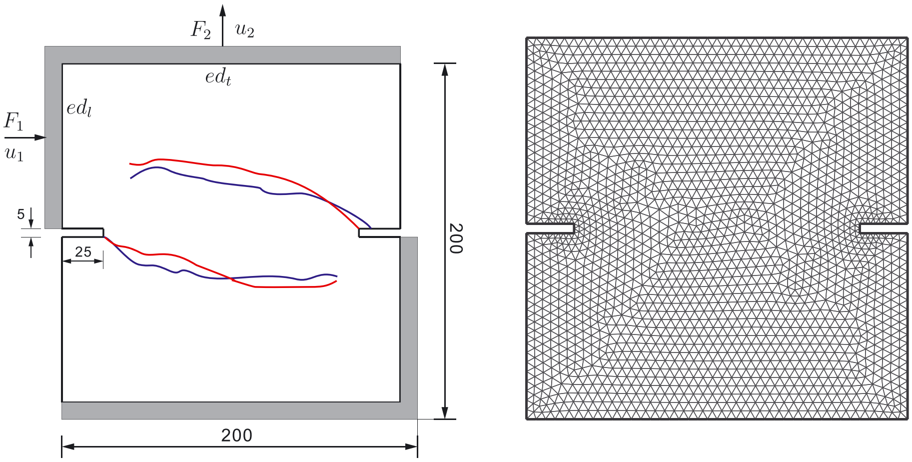

(A) geometry (in mm) and boundary conditions (B) initial triangulation

FIGURE 15 Nooru-Mohamed shear test: geometry, boundary conditions and initial triangulation. The solid lines in A, represent crack paths obtained in the experiment of the case $F_1 = 10\text{kN}$ [Colour figure can be viewed at wileyonlinelibrary.com]

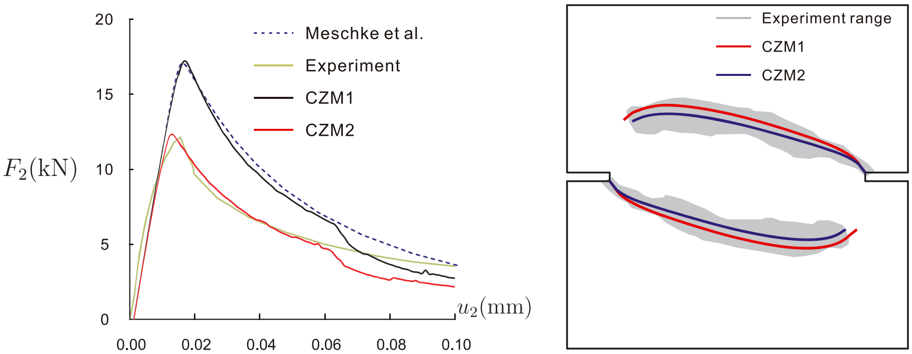

(A) load displacement curve (B) predicted crack path

FIGURE 16 Load-displacement response and predicted crack path [Colour figure can be viewed at wileyonlinelibrary.com]

the exponential decohesion relation in a previous study (29) with two different sets of values for the tensile strength and the fracture energy: (1) $t_u = 3.0$MPa, $\mathcal{G}_c = 0.11$ N/mm, labelled as "CZM1",[51] and (2) $t_u = 2.3$MPa, $\mathcal{G}_c = 0.08$ N/mm labelled as "CZM2."[52] Herein, we include mode-II behaviour: $d_{\text{int}} = 10$N/mm and $h_s = 0$ in Equation 29.[53] Plane-stress conditions are assumed and the loading condition is set up as follows:

Step 1 Load control is considered to fully track the load-displacement path with steps of $\Delta F_1 = 2$kN along the upper left edge ed_l. The top edge ed_t is fixed at this stage, see Figure 15A. To achieve this, a prescribed horizontal displacement u_1 has been applied along the upper left edge. These displacement boundary conditions are applied as Equation 32 for all the Powell-Sabin triangle corners associated with the vertices along the upper left edge ed_l and the top edge ed_t. Then, we sum up all internal forces along the upper left edge ed_l and add the following relation as a constrain to the system equation.

$$\sum \mathbf{K}_l \Delta \mathbf{U}_l = \Delta u_1 \sum \mathbf{K}_l \begin{bmatrix} 1 & 1 & \cdots & 1 \end{bmatrix}^{\mathrm{T}} = \Delta F_1, \tag{33}$$

where $\mathbf{K}_l$ represents the stiffness matrix associated with degrees of freedom of Powell-Sabin triangle corners along the upper left edge ed_l, see Figure 15A; $\Delta \mathbf{U}_l$ denotes the displacement increment of degrees of freedom along the upper left edge ed_l. Δu_1 represents the prescribed displacement increment along the upper left edge ed_l.

Step 2 Displacement control is employed to fully track the load-displacement path with steps of $\Delta u_2 = 0.001$mm along the top edge ed_t, while keeping $F_1 = 10$kN constant along the upper left edge ed_l, see Figure 15A. This is achieved by applying the displacement boundary condition along the top edge ed_t as in Equation 32, for all the Powell-Sabin triangle corners. The displacement boundary condition along the upper left edge ed_l is computed following:

$$\sum \mathbf{K}_l \mathbf{U}_l = u_1 \sum \mathbf{K}_l \begin{bmatrix} 1 & 1 & \cdots & 1 \end{bmatrix}^{\mathrm{T}} = F_1 = 10\text{kN}, \tag{34}$$

which will be considered as a constraint on the system of equation.

The response curve is given in terms of the vertical load F_2 vs the vertical displacement u_2, see Figure 16A. For the parameter set CZM1, the numerical results deviate from the experimental observations. The difference is caused by the overestimation of fracture parameters t_u and $\mathcal{G}_c$.[51] For the parameter set CZM2, the results agree well with the experimental results.[50] There is a discrepancy between the simulation and the experimental results in the tail of the load-dispacement curve. This is because of the fact that we do not consider the mixity of crack modes.[51] For the initial part of the crack simulation, the mixity is not so important, but becomes relevant later on. In Figure 17, the meshes at different load steps are given. As expected, the meshes are well defined with good aspect ratios. The stress contours for different load levels are given in Figure 18. The crack propagates gradually when increasing the vertical displacement u_2. A comparison of the computed crack path and the experimental results (shaded in grey) is given in Figure 16B. Compared with standard finite element methods, the present method can provide a smoother crack path and load-displacement curve due to the C^1 continuous basis functions.[54] Furthermore, elements with higher continuity tend to result in a more accurate stress tensor, which in turn will better predict the direction of the crack path.

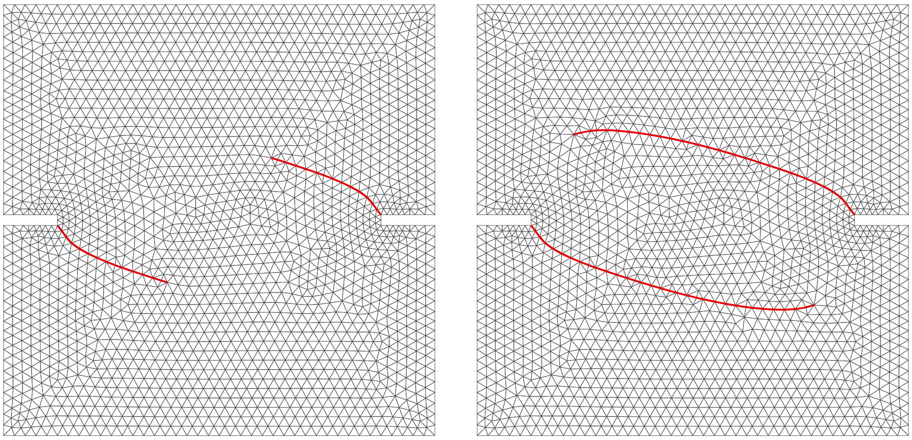

(A) mesh at load step $u_2 = 0.13$mm (B) mesh at load step $u_2 = 0.94$mm

FIGURE 17 Mesh in the deformed configuration. The red lines indicate the crack path, which is aligned with the triangle element boundaries [Colour figure can be viewed at wileyonlinelibrary.com]

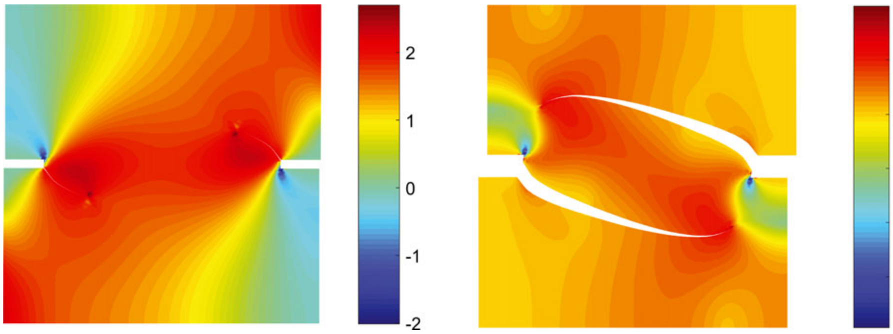

(A) σ_1 contour plot for $u_2 = 0.01$mm (B) σ_1 contour plot for $u_2 = 0.09$mm

FIGURE 18 Stress distribution σ_1(MPa) for different load steps. The parameter set is considered. The displacements have been amplified by a factor 100 [Colour figure can be viewed at wileyonlinelibrary.com]

5 | CONCLUSIONS

For a number of applications in fracture of concrete and rock, discrete modelling is to be preferred. Recently, isogeometric analysis has been used for this purpose and crack segments are then represented by NURBS or T-spline basis functions.[16,17,19-23] Indeed, the higher-order continuity of the NURBS and T-spline shape functions that are employed, result in the advantageous property of smooth and accurate stress fields.

Nevertheless, NURBS and T-splines have some limitations when modelling (cohesive) fracture, and a discrete representation of a crack fails in some situations. This restriction is because of the fact that the crack segment is inserted in the parameter domain and that a reparametrisation must be carried out in the physical domain. Moreover, the degree of continuity of NURBS and T-splines is reduced to C^0 at the crack tip, which necessitates to use the stresses at integration points around the crack tip to assess whether the criterion for insertion of a new crack segment has been met.

The use of Powell-Sabin B-splines, which are based on triangles, overcomes these restrictions. In this approach, a crack is introduced directly in the physical domain. Moreover, Powell-Sabin B-splines remain C^1 continuous at the crack tip, which allows for assessing the crack initiation criterion at this point. Furthermore, remeshing is straightforward because of the use of triangles. The initial mesh does not have to be aligned with the final crack path, which can be the case for isogeometric analysis. To ensure compatibility with existing finite element programmes, an element-wise point of view is adopted through the use of Bézier extraction. Numerical examples show that the refinement ability of the Powell-Sabin B-splines is very suitable for the analysis of crack propagation.

A limitation of Powell-Sabin B-splines lies in the extension to three-dimensional objects. Until now, there is no procedure to define Powell-Sabin B-splines on arbitrary tetrahedral meshes because of certain constraints with neighbouring tetrahedrons,[55,56] and they only work for structured meshes. Alternatively, one can construct prisms as a tensor product of two-dimensional Powell-Sabin B-splines and NURBS in the third dimension.

ACKNOWLEDGEMENTS

Financial support from the European Research Council (Advanced Grant 664734 "PoroFrac") is gratefully acknowledged.

ORCID

René de Borst https://orcid.org/0000-0002-3457-3574

REFERENCES

1. de Borst R. Some recent issues in computational failure mechanics. *Int J Numer Methods Eng*. 2001;52:63-95.
2. de Borst R, Remmers JJC, Needleman A, Abellan MA. Discrete vs smeared crack models for concrete fracture: bridging the gap. *Int J Numer Anal Methods Geomech*. 2004;28:583-607.
3. Li B, Millán D, Torres-Sánchez A, Roman B, Arroyo M. A variational model of fracture for tearing brittle thin sheets. *J Mech Phys Solids*. 2018;119:334-348.
4. Dugdale DS. Yielding of steel sheets containing slits. *J Mech Phys Solids*. 1960;8:100-104.
5. Barenblatt GI. The mathematical theory of equilibrium cracks in brittle fracture. *Adv Appl Mech*. 1962;7:55-129.
6. Xu XP, Needleman A. Void nucleation by inclusion debonding in a crystal matrix. *Modell Simul Mater Sci Eng*. 1993;1:111-132.
7. de Borst R. Numerical aspects of cohesive-zone models. *Eng Fract Mech*. 2003;70:1743-1757.
8. Allix O, Ladevèze P. Interlaminar interface modelling for the prediction of delamination. *Compos Struct*. 1992;22:235-242.
9. Schellekens JCJ, de Borst R. On the numerical integration of interface elements. *Int J Numer Methods Eng*. 1993;36:43-66.
10. Balzani C, Wagner W. An interface element for the simulation of delamination in unidirectional fiber-reinforced composite laminates. *Eng Fract Mech*. 2008;75:2597-2615.
11. Camacho GT, Ortiz M. Computational modelling of impact damage in brittle materials. *Int J Solids Struct*. 1996;33:2899-2938.
12. Secchi S, Simoni L, Schrefler BA. Mesh adaptation and transfer schemes for discrete fracture propagation in porous materials. *Int J Numer Anal Methods Geomech*. 2007;31:331-345.
13. Wells GN, Sluys LJ. A new method for modelling cohesive cracks using finite elements. *Int J Numer Methods Eng*. 2001;50:2667-2682.
14. Wells GN, de Borst R, Sluys LJ. A consistent geometrically non-linear approach for delamination. *Int J Numer Methods Eng*. 2002;54:1333-1355.
15. Remmers JJC, de Borst R, Needleman A. The simulation of dynamic crack propagation using the cohesive segments method. *J Mech Phys Solids*. 2008;56:70-92.
16. Verhoosel CV, Scott MA, de Borst R, Hughes TJR. An isogeometric approach to cohesive zone modeling. *Int J Numer Methods Eng*. 2011;87:336-360.
17. Irzal F, Remmers JJC, Verhoosel CV, de Borst R. An isogeometric analysis Bézier interface element for mechanical and poromechanical fracture problems. *Int J Numer Methods Eng*. 2014;97:608-628.
18. Dimitri R, De Lorenzis L, Wriggers P, Zavarise G. NURBS and T-spline-based isogeometric cohesive zone modeling of interface debonding. *Comput Mech*. 2014;54:369-388.
19. Vignollet J, May S, de Borst R. On the numerical integration of isogeometric interface elements. *Int J Numer Methods Eng*. 2015;102:1773-1749.
20. Vignollet J, May S, de Borst R. Isogeometric analysis of fluid-saturated porous media including flow in the cracks. *Int J Numer Methods Eng*. 2016;108:990-1006.
21. May S, de Borst R, Vignollet J. Powell-Sabin B-splines for smeared and discrete approaches to fracture in quasi-brittle materials. *Comput Meth Appl Mech Eng*. 2016;307:193-214.
22. Chen L, Lingen FJ, de Borst R. Adaptive hierarchical refinement of NURBS in cohesive fracture analysis. *Int J Numer Methods Eng*. 2017;112:2151-2173.
23. Chen L, Verhoosel CV, de Borst R. Discrete fracture analysis using locally refined T-splines. *Int J Numer Methods Eng*. 2018;116:117-140.
24. Chen L, de Borst R. Locally refined T-splines. *Int J Numer Methods Eng*. 2018;114:637-659.
25. Powell MJ, Sabin MA. Piecewise quadratic approximations on triangles. *ACM Trans Math Software (TOMS)*. 1977;3:316-325.
26. Dierckx P, Van Leemput S, Vermeire T. Algorithms for surface fitting using Powell-Sabin splines. *IMA J Numer Anal*. 1992;12:271-299.
27. Vanraes E, Windmolders J, Bultheel A, Dierckx P. Automatic construction of control triangles for subdivided Powell-Sabin splines. *Comput Aided Geom Des*. 2004;21:671-682.
28. May S, Vignollet J, de Borst R. Powell-Sabin B-splines and unstructured standard T-splines for the solution of Kichhoff-Love plate theory using Bézier extraction. *Int J Numer Methods Eng*. 2016;107:205-233.

29. O'Rourke J, Aggarwal A, Maddila S, Baldwin M. An optimal algorithm for finding minimal enclosing triangles. *J Algorithms*. 1986;7:258-269.
30. Ito Y, Nakahashi K. Direct surface triangulation using stereolithography data. *AIAA J*. 2002;40:490-496.
31. Wang D, Hassan O, Morgan K, Weatherill N. Enhanced remeshing from STL files with applications to surface grid generation. *Commun Numer Methods Eng*. 2007;23:227-239.
32. Borouchaki H, Laug P, George P-L. Parametric surface meshing using a combined advancing-front generalized Delaunay approach. *Int J Numer Methods Eng*. 2000;49:233-259.
33. Marcum DL. Efficient generation of high-quality unstructured surface and volume grids. *Eng Comput*. 2001;17:211-233.
34. Attene M, Falcidieno B, Spagnuolo M, Wyvill G. A mapping-independent primitive for the triangulation of parametric surfaces. *Graphical Models*. 2003;65:260-273.
35. Marcum DL, Gaither JA. Unstructured surface grid generation using global mapping and physical space approximation. In: IMR; 1999; South Lake Tahoe, California. 397-406.
36. MATLAB. *Version 9.2.0.556344 (R2017a)*. Natick, Massachusetts: The MathWorks Inc.; 2017.
37. Mosek A. The MOSEK optimization software. Online at http://www.mosek.com; 2010.
38. Bochkanov S, Bystritsky V. Alglib-a cross-platform numerical analysis and data processing library. ALGLIB Project; 2011.
39. Chen L, de Borst R. Adaptive refinement of hierarchical T-splines. *Comput Meth Appl Mech Eng*. 2018;337:220-245.
40. Giorgiani G, Guillard H, Nkonga B. A Powell-Sabin finite element scheme for partial differential equations. *ESAIM: Proc*. 2016;53:64-76.
41. Funken S, Praetorius D, Wissgott P. Efficient implementation of adaptive P1-FEM in Matlab. *Comput Methods Appl Math*. 2011;11:460-490.
42. Klinkel S, Chen L, Dornisch W. A NURBS based hybrid collocation – Galerkin method for the analysis of boundary represented solids. *Comput Meth Appl Mech Eng*. 2015;284:689-711.
43. Chen L, Dornisch W, Klinkel S. Hybrid collocation – Galerkin approach for the analysis of surface represented 3D-solids employing SB-FEM. *Comput Meth Appl Mech Eng*. 2015;295:268-289.
44. Chen L, Simeon B, Klinkel S. A NURBS based Galerkin approach for the analysis of solids in boundary representation. *Comput Meth Appl Mech Eng*. 2016;305:777-805.
45. Yosibash Z. *Singularities in Elliptic Boundary Value Problems and Elasticity and their Connection with Failure Initiation*, Vol. 37. Berlin: Springer; 2011.
46. de Borst R, Chen L. The role of Bézier extraction in adaptive isogeometric analysis: Local refinement and hierarchical refinement. *Int J Numer Methods Eng*. 2018;113:999-1019.
47. Winkler BJ. *Traglastuntersuchungen von Unbewehrten und Bewehrten Betonstrukturen auf der Grundlage eines Objektiven Werkstoffgesetzes Für beton*. Innsbruck: Innsbruck University Press; 2001.
48. Unger JF, Eckardt S, Könke C. Modelling of cohesive crack growth in concrete structures with the extended finite element method. *Comput Meth Appl Mech Eng*. 2007;196:4087-4100.
49. Belytschko T, Fleming M. Smoothing, enrichment and contact in the element-free Galerkin method. *Comput Struct*. 1999;71:173-195.
50. Nooru-Mohamed MB. Mixed-mode fracture of concrete: an experimental approach. *Ph.D. Thesis*. Delft: Delft University of Technology; 1992.
51. Meschke G, Dumstorff P. Energy-based modeling of cohesive and cohesionless cracks via X-FEM. *Comput Meth Appl Mech Eng*. 2007;196:2338-2357.
52. Wang Y, Waisman H. From diffuse damage to sharp cohesive cracks: A coupled XFEM framework for failure analysis of quasi-brittle materials. *Comput Meth Appl Mech Eng*. 2016;299:57-89.
53. Xu Y, Yuan H. Applications of normal stress dominated cohesive zone models for mixed-mode crack simulation based on extended finite element methods. *Eng Fract Mech*. 2011;78:544-558.
54. Jirásek M. Comparative study on finite elements with embedded discontinuities. *Comput Meth Appl Mech Eng*. 2000;188:307-330.
55. Worsey AJ, Piper B. A trivariate Powell-Sabin interpolant. *Comput Aided Geometric Des*. 1988;5:177-186.
56. Sorokina T, Worsey AJ. A multivariate Powell-Sabin interpolant. *Adv Comput Math*. 2008;29:71-89.

How to cite this article: Chen L, de Borst R. Cohesive fracture analysis using Powell-Sabin B-splines. *Int J Numer Anal Methods Geomech*. 2019;43:625–640. https://doi.org/10.1002/nag.2882